Type of paper: full length article (Powder Technology - Elsevier Journal)
Date text written: April 2019
Date text revised: July 2019
Number of words in main text and tables = 5625
Number of figures = 15
Number of tables = 2

Impact of three-dimensional sphericity and roundness on heat transfer in granular materials

Author 1
Wenbin Fei, PhD student, ME, BE
Department of Infrastructure Engineering, The University of Melbourne, Parkville, Australia

Author 2
Guillermo A. Narsilio✉, PhD, MSc (Math), MSc (CE), CEng
Department of Infrastructure Engineering, The University of Melbourne, Parkville, Australia

Author 3
Mahdi M. Disfani, PhD, MSc, BSc
Department of Infrastructure Engineering, The University of Melbourne, Parkville, Australia

Abstract

Knowledge of particle morphology is vital to understand the behaviour of natural geomaterials including heat transfer. The effects of particle shape on heat transfer have been mostly quantified with two-dimensional (2D) particle descriptors or at most with a single three-dimensional (3D) descriptor. However, these particle shape descriptors may fail to capture the shape of all irregular particles. To redress this issue, we developed a method to reconstruct particles from micro-computed tomographic (μCT) images and to extract 3D sphericity and roundness of individual particles in the assembly. Sphericity and roundness of five real sand packings are calculated using the new proposed method. Furthermore, the effective thermal conductivity (ETC) of each sample is estimated using finite element modelling. Our results show that packings with higher sphericity or roundness tend to render higher ETC. A further examination of the microstructure in the assemblies indicates that sphericity or roundness corresponds to inter-particle contacts.

Keywords: Heat transfer, Particle shape, Granular material, Particle reconstruction.

Graphic abstract

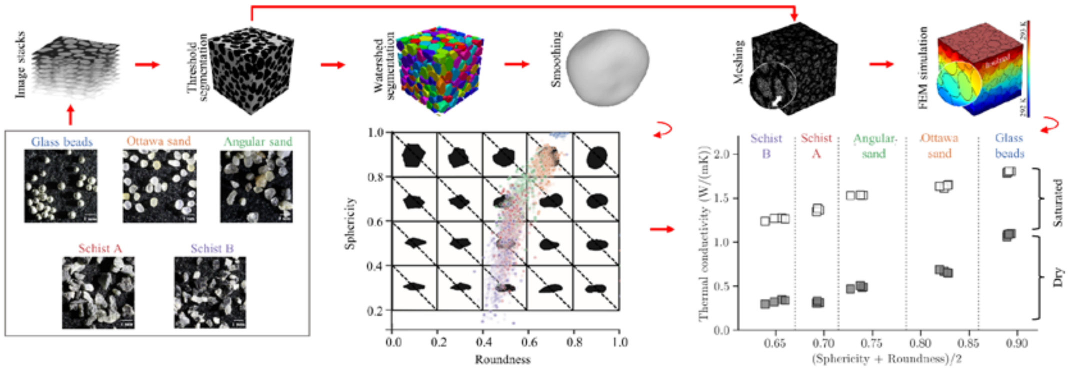

Five granular materials of similar particle size but different shape are scanned. From the resulting micro-CT images, the particle shape of each individual particle is automatically computed using an algorithm introduced here that comprises a series of steps shown on the top row, resulting in now well-defined Sphericity and Roundness shown in the bottom middle figure. The thermal conductivity of each material is calculated using particle scale FEM to finally unveil the relationship between particle shape and thermal conductivity, as shown in the bottom right.

1 Introduction

Knowledge of effective thermal conductivity (λ_{eff}) of granular systems, for example, is required in design, prediction and control of processes in many engineering applications such as radioactive waste disposal [1], geological carbon dioxide storage [2], hydrocarbon energy [3] and geothermal engineering [4]. As the λ_{eff} is affected by the microstructure [5, 6] in the granular materials, to quantify the impact of microstructural features on λ_{eff} enhances the fundamental understanding of heat transfer processes. Particle shape is a fundamental feature in characterising the microstructure of natural soils and rocks. Hence, it is vital to fundamentally understand how particle shape affects the λ_{eff} of these geomaterials and of other granular materials.

Many experiments and simulations show that particle shape contributes significantly to the mechanical [7-10], hydraulic [11-14] and thermal [15-17] behaviour of geomaterials. Even though the correlation between particle shape and λ_{eff} has been quantified by introducing two-dimensional (2D) particle descriptors [15, 18], the easily measured 2D particle shape descriptors [10, 19-21] (e.g., circularity, sphericity, roundness, aspect ratio, convexity, compactness and solidity) can be random and inaccurate as they may depend on the projection direction. This is particularly the case for irregular and platy particles. The relationship between particle shape and thermal conductivity were also studied by using three-dimensional (3D) sphericity to characterise the particle shape [22, 23]. However, (synthetic) particles with only a certain shape such as sphere and cylinder were selected for those studies. Moreover, the 3D sphericity defined [24] as the ratio of the surface area of the equivalent sphere of a particle to the real surface area of the particle can be used to represent the particle shape. However, this sphericity definition cannot distinguish, for example, between particles with a disc-shape and particles with a rod-shape. Discrete element method (DEM) has also been used to generate ellipsoids varying in aspect ratio to study the effect of particle shape on λ_{eff} [17]. However, the artificial ellipsoid or supper-ellipsoid [25] from DEM are different from many real natural sands. As other definitions of sphericity [24, 26-29] and other 3D particle shape descriptors such as roundness [24] are available, these 3D particle shape descriptors (and definitions) should be identified and chosen carefully to ensure they can properly describe *all* possible irregular particles in a packing or assembly.

Particle shape and particle arrangement (i.e., microstructure) influence the behaviour of the assemblies. To rigorously study their impact on the thermal (and other) response of geomaterials, one would prefer to derive shape descriptors from the same sample (and of the particle assembly) for testing thermal parameters. Since particle shape descriptors are calculated based on the particle geometry, individual particles should be extracted from the particle assembly without disturbing the structure of the sample rather than selecting a few representative particles from the sample. Techniques such as resin impregnation and sequential 2D (physical) slicing and polishing of surfaces throughout the sample and the use of common microscopic facilities are effective but time and labour intensive, and destroy the samples [20, 30, 31]. Alternatively, X-ray computed tomography (CT) is one of the non-destructive image techniques able to visualise 3D particles in the samples [32-34]. Even though CT techniques have been used in the study of mechanical response [35, 36] and fluid flow [37] in granular materials, they have rarely been applied to the study of heat transfer. CT techniques can generate sequential cross-sectional images of the geomaterial at a certain interval (image resolution) and the solid phase can be detected based on the greyscale of each image. From the stacking of the solid phase in all images, one can construct a "voxelated" geometry. However, the particles in the geometry may overestimate [38] the inter-particle contact area and even appear or cemented to each other. As the contact area is related to the thermal conductance [39], post-processing image techniques are required to identify "true" individual particles.

Based on the collection of individual particles extracted from voxel-constructed geometry, the particle surface area can be measured using the boundary voxels, and the particle volume can be computed based on the number of voxels inside each particle [38, 40]. However, the voxelated particle surface has a saw-tooth pattern and overlapping voxels, leading to an overestimation [38] which means the computed value may further affect the accuracy of measuring sphericity and roundness. Moreover, since 3D roundness are widely accepted [24, 27, 41] as the ratio of the average radius of the particle corners and the radius of the maximum inscribed circle, the voxel-constructed particle surface cannot be used to calculate the correct curvature for identifying the corners. Consequently, smoothing the voxel-constructed particles before calculating the 3D sphericity and roundness is required. These issues will be addressed in the present study.

The study aims to investigate the effect of particle shape on the effective thermal conductivity of granular materials. To achieve this, various particle shape descriptors are compared to then determine a combination of shape descriptors that can actually cover particle with a wide range of different shapes. Moreover, the theories used to compute the selected particle shape descriptors are explained. A framework is introduced to generate individual smooth particles based on CT images and the methodology is exemplified using five real sand packings. The experimental and numerical methods used to measure the effective thermal conductivity are explained in detail, followed by quantitative analysis on how and why particle shape and microstructure affect heat transfer in granular materials.

2 Particle shape descriptors

Particle shape can be generally described at three different length scales [7] (Fig. 1): Sphericity/Elongation, Roundness/Angularity and Smoothness/Roughness. At the scale of the equivalent particle diameter, sphericity indicates the global form of the particle and describes the proximity of a particle to a sphere while elongation describes the opposite trend. At approximately one tenth of the scale of the equivalent particle diameter, roundness characterises the particle shape at a smaller scale than the scale of sphericity. Roundness is a local feature and represents the extent to which the corners and edges of the particle have been rounded, its counterparty is known as angularity. Smoothness or roughness describes the smallest scale and indicates the platenenss of the particle surface. Since images with resolution higher than 1 μm [42] are typically required to calculate the roughness, the present work focuses on the implementation of sphericity and roundness because the resolution of CT scans is typically lower. The CT scanned images used in this work, for example, have a resolution of approximately 13 μm.

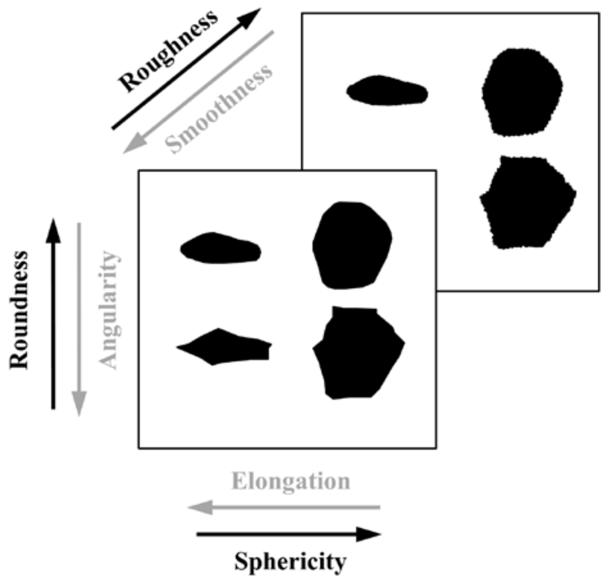

Fig. 1 Particle shape descriptors at three different scales: Sphericity, Roundness and Smoothness.

2.1 Three-dimensional sphericity and roundness

A number of definitions (and corresponding equations) have been proposed in the literature to calculate three-dimensional (3D) sphericity and roundness. Table 1 summarises some of these definitions and formulae to compute 3D sphericity (S1 – S5) employing different parameters. While particle volume V and surface area SA are used in S1 and S2, the radius of maximum inscribed and minimum circum-scribed sphere ($r_{max\text{-}in}$ and $r_{min\text{-}cir}$, respectively) are adopted in S3. The length of principal axes of the particle d_i is employed in S4 and S5. However, none of these descriptors can distinguish all particles with different shapes. For example, S1 and S2 cannot distinguish between disc-shape particles and rod-shape particles because they may have the same surface area and volume, as depicted in Fig. 2(a). In Fig. 2(b) and Fig. 2(c) S3 cannot recognise the difference between particle 1 and particle 2 because they have the same maximum inscribed circle and the minimum circum-scribed circle. Moreover, S4 and S5 cannot distinguish particle 1 and particle 2 in Fig. 2(c) since they have the same principle axes if considering the two particles have the same thickness in 3D.

Table 1 A summary of various definitions of sphericity

Notation	Equation	Description	Reference
S1	$\frac{\sqrt[3]{36\pi V^2}}{\mathrm{SA}}$	The ratio of the surface area of the equivalent sphere of a particle to the real surface area of the particle. V is particle volume and SA is particle surface area.	[24]
S2	$\frac{36\pi V^2}{\mathrm{SA}^3}$	The cubic order of S1.	[26]
S3	$\frac{\mathrm{r_{max-in}}}{\mathrm{r_{min-cir}}}$	The ratio of the radius $\mathrm{r_{max-in}}$ of the maximum inscribed circle (sphere in 3D) to the radius ($\mathrm{r_{min-cir}}$) of the minimum circum-scribed circle of a particle shown in Fig. 2(b).	[27]
S4	$\frac{\mathrm{d_S}}{d_L}$	The ratio of the maximum axial length ($\mathrm{d_S}$) to the minimum axial length ($\mathrm{d_L}$) of a particle.	[28]
S5	$\sqrt[3]{\frac{d_S^2}{d_L d_I}}$	Fitting a particle to an ellipsoid, $\mathrm{d_S}$, $\mathrm{d_I}$ and $\mathrm{d_L}$ are the shortest, intermediate and the longest axial length of the fitted ellipsoid.	[29]

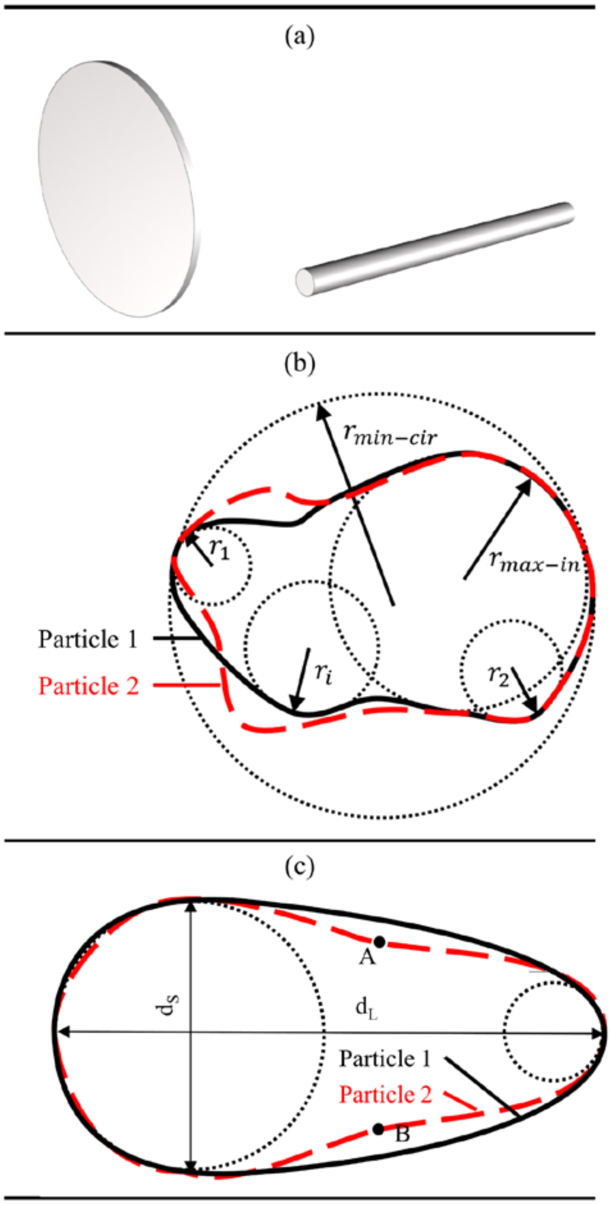

Fig. 2 Examples of potential shortcomings of the various definitions of sphericity and roundness: (a) Example of two particles of different shape but same sphericity (S1 and S2 in Table 1); (b) Example of two particles of different shape but same sphericity (S3 in Table 1) and roundness. (c) Example of two particles of different shape but same sphericity (S4 and S5 in Table 1) and roundness

In contrast to the various definitions of sphericity, only few equations have been proposed to compute 3D roundness. Equation 1 below is used to calculate 3D roundness as the ratio of the average radius of the particle corners to the radius of the maximum inscribed sphere (see Fig. 2(b)):

$$R = \frac{\sum r_i/N}{r_{max-in}} \tag{1}$$

where r_i is the radius of corners in a particle as shown in Fig. 2(b), N is the total number of corners and r_{max-in} is the maximum inscribed circle of a particle. However, the roundness of the particles in Fig. 2(c) cannot be distinguished if neglecting the local feature on particle surface where the radius of curvature is larger than the maximum inscribed circle.

Since neither sphericity nor roundness alone can distinguish *all* particles with different shapes, combinations of sphericity and roundness have been used to ensure that all particles with various shapes can be identified [41]. From the previous explanation, particles shown in Fig. 2(c) still cannot be distinguished even if roundness is combined with sphericities S4 or S5. Furthermore, S3 cannot distinguish the two particles in Fig. 2(c), hence using roundness with S3 still fails to recognise the two different particles. Consequently, the remaining S1 and S2 definitions are good candidates which together with roundness could characterise particle shape unambiguously.

To analyse the performance of S1 and S2, a hexahedron with dimensions $L_1 \times L_2 \times L_3$ is adopted but keeping L_1 equal to L_2 and then changing the ratio of L_3 to L_1. According to the results in Fig. 3, a hexahedron with L_3/L_1 varying between 1 and 7, shows a sphericity that shifts from 0.81 to 0.59 when using definition S1, while it changes from 0.52 to 0.21 when using definition S2. Since sphericity is conceptually defined as the proximity of a particle shape to a sphere (sphericity is 1) and a hexahedron with $L_3/L_1 = 7$ is far from a sphere, assigning 0.59 to the sphericity of such an elongated particle may be intrinsically unacceptable, as one would expect a much lower value.

As a consequent of the above discussions, in this work sphericity as defined in S2 in Table 1 and roundness as defined in Equation 5 are selected as the combination of descriptors to better characterise the shape of particles in natural granular materials like sands.

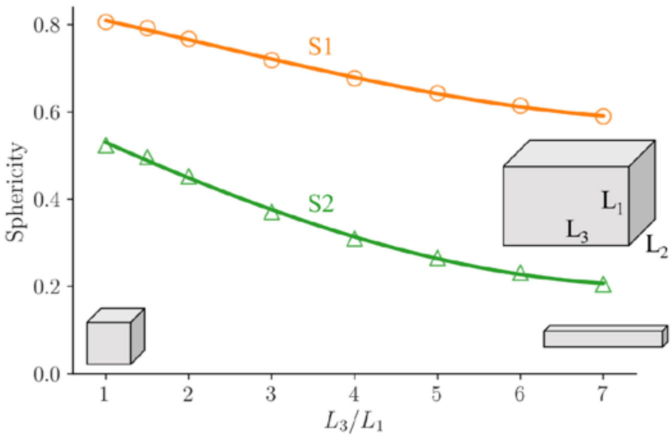

Fig. 3 Comparison of sphericity S1 and S2 defined in Table 1 of a hexahedron with varying dimensions (L_1=L_2, $1 \leqslant L_3/L_1 \leqslant 7$)

2.2 *Calculation of sphericity and roundness*

From the last section, it is known that the particle surface area and volume are required to compute sphericity whereas curvature is required for calculating roundness. While Fiji [43] is available to compute the particle surface area and volume, the computations are based on voxel-constructed particles which have saw-tooth boundary patterns. The saw-tooth boundary patterns may lead to overestimation of real particle surface area and an incorrect calculation of curvature, the computation of sphericity and roundness should be based on smooth particles. However, no commercial software or open-source code is available to achieve smooth particle geometry and calculate 3D sphericity and roundness using the equations we selected. In this work, we first identify each individual particle and then the smoothing particle surface is made up of triangle surface meshes (similar to [41] as shown in Fig. 4(a). Therefore, the surface area of each facet on the particle surface is easily computed, and the summation of all the triangular facet areas is the surface area of the particle (Fig. 4(b)). To compute the individual particle volume, the following procedure is followed. A point inside the particle together with the three points of a single triangular facet form a tetrahedron, so the total volume of the tetrahedrons related to all facets is the particle volume (Fig. 4(b)). Thus, to calculate the particle surface area and volume, Equations 2 and 3 are used. Given particle volume and surface area, then S2 can be calculated as the sphericity of each particle.

$$SA = \sum_{i=1}^{n} \frac{1}{2} \left| \overrightarrow{A_i B_i} \times \overrightarrow{B_i C_i} \right| \tag{2}$$

$$V = \sum_{i=1}^{n} \frac{1}{6} \left| \overrightarrow{OA_i} \cdot \left(\overrightarrow{OB_i} \times \overrightarrow{OC_i} \right) \right| \tag{3}$$

where O is the particle centre calculated as the average coordinates of all vertices in the particle, A_i, B_i and C_i are three vertices of the i^{th} triangular facet and n is the total number of the facets on the particle surface.

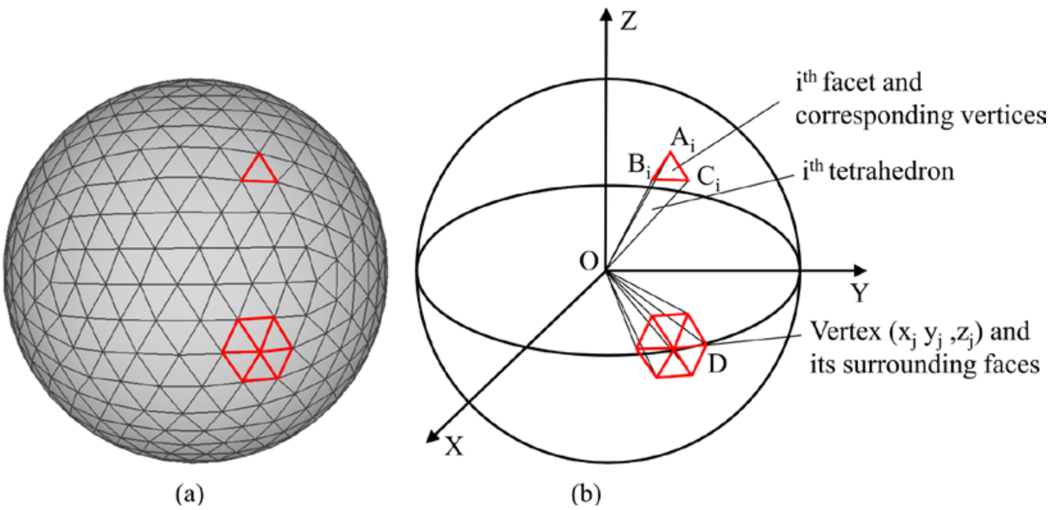

Fig. 4 A particle surface is made up of triangular meshes. (a) Triangular meshes of a sphere, (b) A diagram to illustrate the principles of computing particle surface area, volume and curvature at vertices (after [41]).

To calculate the roundness of a particle, the first step is to identify corners in the particle. An available criterion is that considering a vertex as a corner when its radius of curvature is smaller than the maximum inscribed sphere. The principal curvatures (the maximum curvature $\kappa_{\max}$ and minimum curvature $\kappa_{\min}$) are two common measurements [44], and quadratic fitting in MeshLab [45] can be used to compute them at all vertices. The key of this method is to use rings of a vertex (e.g., the first ring of vertex D in Fig. 4(b) is composed of the six vertices around it) to fit a micro-surface by generating a quadratic polynomial equation. Based on the equation, a Hessian matrix [44] can be established and the eigenvalues of the matrix are the principal curvatures. Subsequently, the principal curvature radii are computed as $r_{\min} = 1/\kappa_{\max}$ and $r_{\max} = 1/\kappa_{\min}$. Between the two radii, $r_{\min}$ is more reasonable to be used for identifying corners because more local features on the particle surface are considered. Then, the corners in a particle can be found using Equation 4.

$$g(k) = \begin{cases} 1 \;\; if \;\; r_{\min} < r_{max-in} \\ 0 \;\; if \;\; r_{\min} \geq r_{max-in} \end{cases} \tag{4}$$

where 1 indicates that the vertex is a corner, while 0 is not, r_{max-in} is the radius of the maximum inscribed sphere of the particle. By introducing *g(k)* into equation 5, the 3D roundness is computed as:

$$R = \frac{\sum g(k) r_{\min} / N}{r_{max-in}} \tag{5}$$

3 Particle reconstruction

3.1 Granular material samples

To test the framework and to analyse the impact of particle shape on effective thermal conductivity, five sands with increasing irregularity of particles are selected (Fig. 5): (a) glass beads are near-spherical particles made from silica; (b) Ottawa sand is sieved to pass No.20 (850μm) mesh and be retained on No.30 (600μm), the achieved 20-30 standard sands are in line with ASTM standard C778 [46]. These particles consist of quartz [47] and are rounded during long-term erosion. (c) an Angular sand also containing a high proportion of quartz with more irregularly shaped particles when compared to the Ottawa sand. (d) Crushed schist sand A is even more irregular than the Angular sand and the particles in Crushed schist A are made of chlorites. (e) Crushed schist B have particles with the most complex shape and more than half of the particles are platy and elongated [48] because they consist of quartz and biotite [49]. The Crushed schist rock B is made from a particular metamorphic rock collected from the Delamarian Fold Belt in western Victoria, Australia. The particle size of each sample is shown in Table 2. Crushed schist rock A and schist rock B are prepared to have the same mean particle size and range in the laboratory.

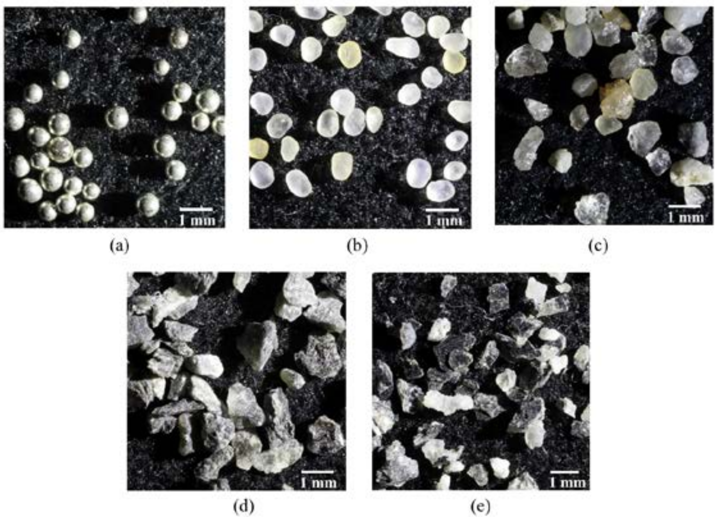

Fig. 5 Micro-pictures of five granular materials with particles of different shape. (a) Glass beads, (b) Ottawa sand, (c) Angular sand, (d) Crushed schist rock A and (e) Crushed schist rock B.

Table 2 Particle size of studied granular materials

Sample	d_{50} (mm) *	d_{50} (mm)^	Particle size range (mm) *	Particle size range (mm) ^
Glass beads	0.60	0.60	0.50 – 0.70	0.40 - 0.80
Ottawa sand	0.73	0.76	0.60 – 0.85	0.58 - 0.94
Angular sand	0.89	0.68	0.60 – 1.18	0.39 – 0.99
Crushed schist rock A	0.84	0.58	0.50 – 1.18	0.23 – 0.95

Crushed schist rock B	0.84	0.61	0.50 – 1.18	0.16 - 1.10

* Diameter from sieve analysis;

^ Equivalent diameter calculated from particle volume using CT reconstruction. Then box plots are drawn, then d_{50} is the median value and particle size range is the range in the box by ignoring the outliers.

These five materials were used to prepare samples in a 25 mm diameter and 25 mm height cylindrical containers made of aluminium using the air-pluviation technique to ensure the homogeneity of the samples and density similarity. The samples are scanned using x-ray computed tomography (CT) to generate sequential grey-scale images with a resolution of 0.013 mm. This resolution lies between the recommendations by Wiebicke, Andò, Herle and Viggiani [50]. Their work suggested that 10-15 µm per voxel and more than 10 pixels across each grain diameter are required to capture the interparticle contact with improved image processing techniques. The greyscale in each voxel represents the image intensity which relates to the density of the scanned materials. Typical cross-sectional image of each sample is shown in Fig. 6. Particles in Glass beads, Ottawa sand and Angular sand samples have similar grey scale even though some defects exist on the boundary of glass beads because of their coating. In contrast, particles in crushed schist rock samples have significant different greyscale because of their complex mineral components.

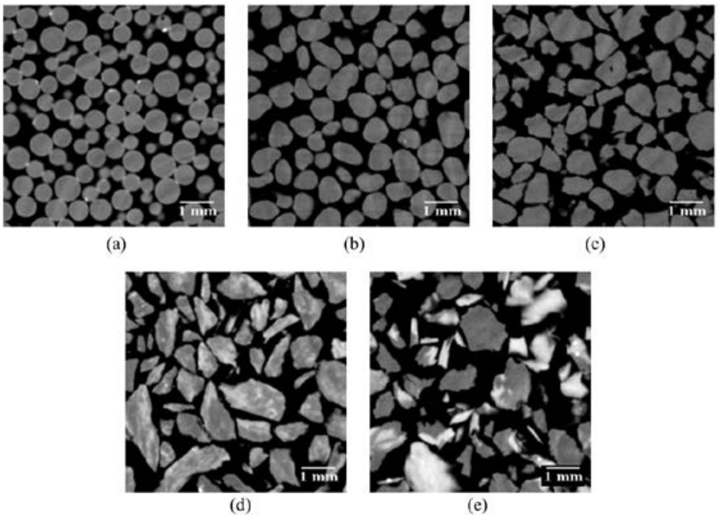

Fig. 6 . CT scanned images of the five granular material packings. (a) Glass beads, (b) Ottawa sand, (c) Angular sand, (d) Crushed schist rock A and (e) Crushed schist rock B

3.2 *Framework*

The geometries of *individual* particles can be acquired using the X-ray CT scans of separate particles placed in a container filled with a (low density) silicon filler [41]. However, identifying individual particles in the samples (i.e., assembly of particles) is not always straightforward. Hence, segmentation is required to identify and extract information of individual particles from the specimen. To accurately calculate 3D sphericity and roundness, a smooth digital particle geometry with the “same” surface area and volume as the real particle is required. Here we combined different techniques and propose a series of steps to reach this goal. This section introduces a framework (Fig. 7) to reconstruct individual smooth particles from a stack of cropped X-ray CT scanned images (Step 1). An open source image processing software Fiji [43] is used to reconstruct the sample micro-geometry (Step 2) and to execute threshold segmentation to identify the solid phase of the particle assemblies (Step 3). Iassonov, Gebrenegus and Tuller [51] applied various threshold segmentation techniques (e.g. local thresholding, global thresholding, region growing methods, deformable surface, probabilistic clustering and Bayesian methods) to porous media. In their work, they found that *local* thresholding can generate satisfactory results but are sensitive to the initial input, while the two *global* threshold segmentation methods (Otsu and the Rilder’s [50, 52-54]) produced satisfactory results without this limitation [38, 50]. Therefore, in our work, the multilevel Otsu threshold segmentation method is applied to the greyscale images. Then a watershed segmentation with 6-connectivity [38, 55] in MorphoLibJ library [26] is adopted to split (“artificially”) connected particles based on the threshold segmentation geometry (Step 3). The 6-connectivity is selected herein because it shows to reduce the overestimation of particle surface area and volume [38]. Boundary particles are discarded because they are part of integral particles resulting from generating the cubic subsamples in Step 1. The individual voxel-constructed particles are thus obtained (Step 5) and then the Taubin smoothing algorithm [56] is used to smooth each particle (Step 6).

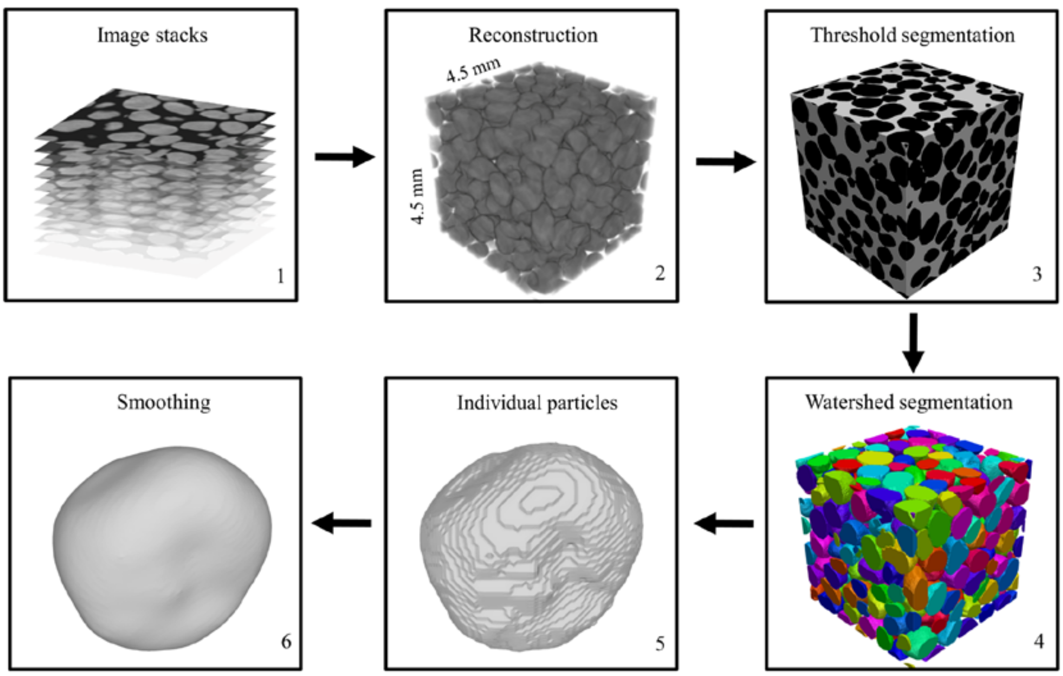

Fig. 7 A framework is used to reconstruct induvial smoothing particles

3.3 *Smoothing method*

In Step 6 of the aforementioned framework, a smoothing algorithm is required to polish the saw-tooth surface of voxelated particles and preserve the general particle morphology. Common iterative mesh smoothing algorithms utilise “processing mesh normals” scheme [57-59]. Most traditional smoothing algorithms, including Gaussian smooth and Laplacian smooth, have a general shrinkage problem which means a particle may collapse to a point when smoothing is implemented for a large number of iterations. Alternatively, the Taubin λ/μ method [56] consists of two Gaussian smoothing algorithms in each step: λ is positive and relates to the shrinkage whereas μ is negative and controls the infatuation.

To identify the proper range of values of input parameters in the Taubin method for our samples, synthetic pixelated image stacks of a sphere and an ellipsoid are generated using the image analysis software Fiji [43], the resolution of these images is set at 0.013 mm, which is the same as the resolution used in the CT of the tested samples. The diameter of the sphere is set as 0.65 mm (50 voxels), and the three-principal axial lengths of the ellipsoid are set at 0.65 mm (50 voxels), 0.39 mm (30 voxels) and 0.26 mm (20 voxels). The resulting cross-section images and 3D voxelated particles are shown in Fig. 8.

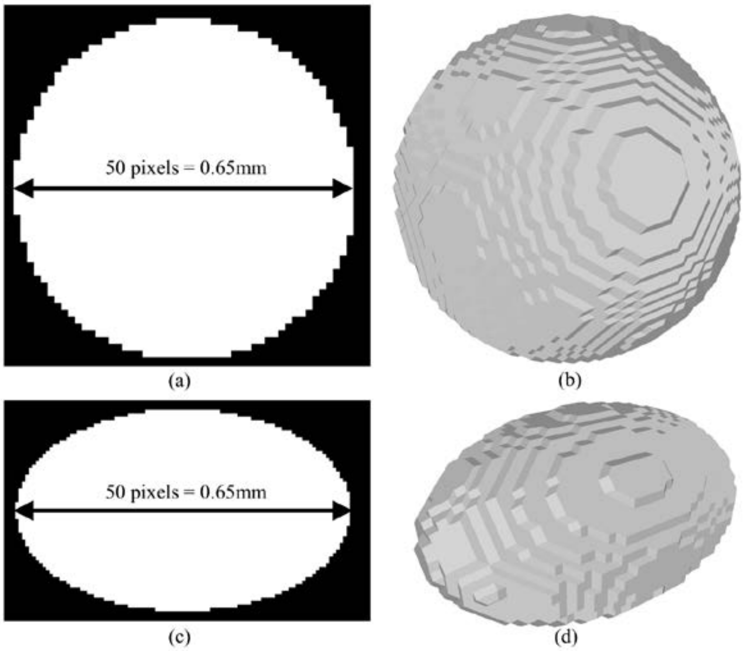

Fig. 8 Voxelated sphere and ellipsoid are constructed from images stacks generated from Fiji: (a) 2D image slice of a sphere, (b) and the resulting voxelated sphere; (c) 2D image slice

of an ellipsoid and (d) the resulting voxelated ellipsoid. The resolution of images is 0.013 mm, same as the resolution of CT scanned images later used int his work

The Taubin smoothing method effectively generates a *low pass filter effect* that is controlled by λ and μ, and the amount of attenuation is then determined by the number of smoothing steps set in the algorithms. The Taubin smoothing method can preserve the geometry of the reconstructed particles from CT images when $\lambda < -\mu$ [56]. Hence, the shrinkage problem in Gaussian smooth and Laplacian smooth is addressed in the Tuabin smoothing method. However, if the surface area and volume from the voxelated particles in the initial step are overestimated to begin with (typical of microCT images), these overestimations are also preserved [38]. To mitigate the initial overestimation of surface area and volume of a particle, $\lambda > -\mu$ is adopted in this work by setting λ as 0.6 and μ as -0.3, which also happen to preserve the geometry of the particles. Together with the synthetic sphere and ellipsoid generated above, two microCT imaged particles, one from the Ottawa sand and one from the Angular sand samples, are also used to investigate the variation of surface area and volume with the number of smoothing steps. Fig. 9 shows that the surface area gradually decreases with smoothing steps, and that the surface area of the voxelated sphere reaches the theoretical value (1.410 mm^2) at the 143rd smoothing step while that of the ellipsoid is reached earlier at the 100th step. As for the reduction of volume, the four particles share a similar trend but at a slower rate of change than that of surface area, the volume of the voxelated sphere reaches the theoretical value (0.41 mm^3) at the 143rd step, which is the same as that of surface area, while the ellipsoid, at the 116th step. In addition to the above analysis to define the range of smoothing steps values that may be appropriate for our studies, sphericity and roundness of Ottawa sand and Angular sand particles are computed and shown in Fig. 10 together with their images at 0, 100 and 200 smoothing steps. It can be seen that the local features of the surface are preserved during the process of Taubin smoothing. Fig. 10 shows that sphericity and roundness converge at early smoothing steps, which is far earlier than the 143rd step found in the previous analysis. To be conservative and to allow a good balance between computational time and accuracy of results, 143 steps (together with λ as 0.6 and μ as -0.3) are selected as input parameters in the smoothing method used herein in the following calculations for all individual particles in natural sands scanned in the micro-CT.

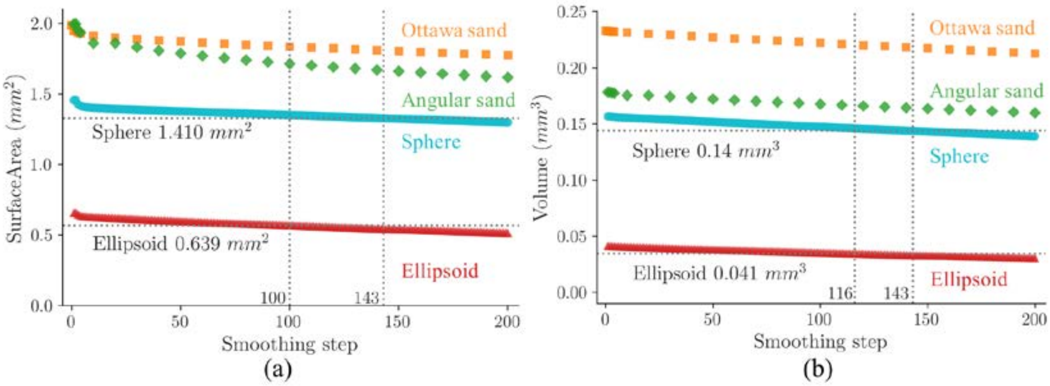

Fig. 9 The surface area (a) and volume (b) decrease gradually with the increase in the number of smoothing steps for $\lambda > -\mu$ in the Taubin smoothing method.

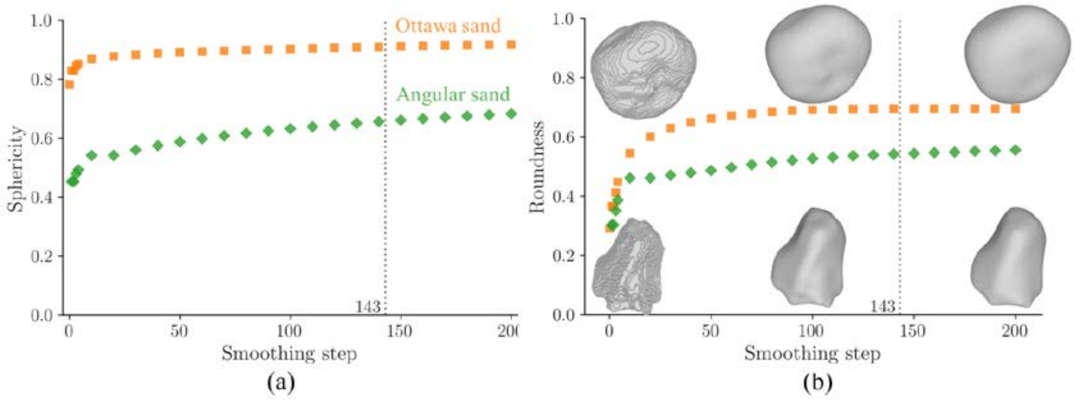

Fig. 10 The sphericity and roundness of two particles from the Ottawa sand and the Angular sand samples as a function of smoothing steps: (a) Sphericity and (b) Roundness. One can also visualize the Ottawa and Angular sand particles at 0, 100 and 200 smoothing steps for comparison

4 Finite element simulation and measurements

The mineral component of a sand can affect its effective thermal conductivity, especially the content of quartz in dry samples [60]. To eliminate this effect, finite element simulation is used in this paper by assigning the same thermal conductivity to the solids of all samples. Experimental measurements, however, are used to validate the numerical results.

4.1 Finite element simulation

The geometry of a sand sample can be reconstructed from scanned CT images and used to simulate heat transfer in a similar fashion as in [61, 62] by numerically solving an elliptic partial differential equation (Equation 6), Fourier's law (Equation 7) and a continuity equation (Equation 8), using COMSOL Multiphysics [63]. The thermal conductivity of the packing are obtained by integrating the heat flux at the top and bottom boundaries using Equation 9, and their average is taken as the effective thermal conductivity of the entire sample.

$$\rho C \frac{\partial T}{\partial t} + \rho C u \cdot \nabla T = \nabla \cdot (\lambda \nabla T) \tag{6}$$

where, for each phase involved in the simulation, ρ is the density (kg/m), C is the heat capacity (J/(kg K)), T is the temperature (K), t is the time (s), u is the velocity vector (m/s), λ is the thermal conductivity (W/(m K)).

$$q = \lambda \nabla T \tag{7}$$

$$-n\left(q_s - q_p\right) = 0 \tag{8}$$

where n is the unit normal vector of the solid-pore interface, q_s and q_p are the heat fluxes in the particle and pore, respectively.

The effective thermal conductivity λ_{eff} ($W\,m^{-1}K^{-1}$) of a sample of horizontal cross-section area A (m^2) is found as:

$$\lambda_{eff} = \frac{\frac{1}{A}\int_A Q_z \, dA}{\frac{T_a - T_b}{L}} \tag{9}$$

where T_a and T_b are the prescribed temperatures at the inlet and outlet boundaries, L (m) is the height of the sample and Q_z (W/m2) is the vertical heat flux of nodes at the inlet or outlet.

The mesh of the Angular sand is shown in Fig. 11(a) and it was generated in Simpleware ScanIP [64] by setting coarseness as -40 after a mesh size sensitivity analysis showed convergence to an asymptotic value of computed thermal conductivity (analysis not included here). The thermal conductivity of minerals has been suggested to be set between 1 and 8 W/(m K) in the literature [61]. Since the aim of this study is on the effect of particle shape on effective thermal conductivity, 3 W/(m K) [39, 65, 66] is assigned to solid particles in all samples to mitigate the potential effects of different mineralogy on the effective thermal conductivity. Thermal conductivity of 0.025 W/(m K) [67] and 0.591 W/(m K) [67] is assigned to the void space within the packings for simulating heat transfer in dry and water-saturated granular materials, respectively[1]. The boundary temperature on the top surface is prescribed at 293 K, while at 292 K on the bottom surface to generate a small thermal gradient, other boundaries are considered as insulation as shown in Fig. 11(b). With this material and boundary conditions, the system is numerically solved for temperature distribution and heat fluxes are estimated to then derive an effective thermal conductivity as described in detail in [61].

[1] Thermal conductivity of bound water may differ from that of free water, while this effect is negligible in coarse grained packings, it may need to be considered in fine grain packings (e.g., clays).

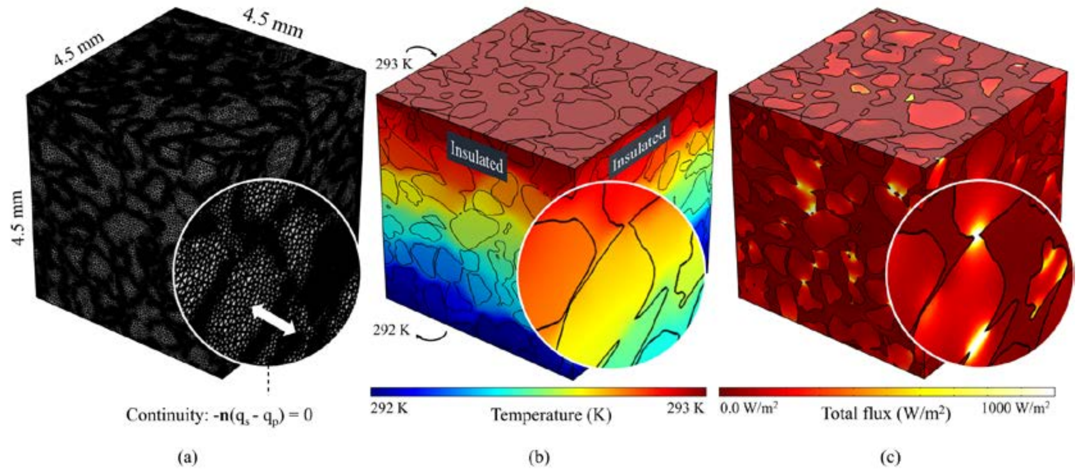

Fig. 11 Finite element mesh and heat transfer simulation results of the Angular sand packing (a) Mesh (b) Temperature distribution and (c) Total heat flux distribution

4.2 Experimental measurements

In order to validate finite element simulating results, the effective thermal conductivity of Ottawa sand, Angular sand and Crushed schist A are measured in the laboratory. Samples are also air-pluviated into a PVC cylindrical container with a diameter of 50 mm and a height of 120 mm to achieve similar homogeneity as shown in the CT images (Fig. 6). The measurements use a 100 mm thermal needle probe (KD2 Pro thermal properties analyser from Decagon Devices, Inc) following ASTM standard D5334-14 [68]. The thermal needle has a diameter of 2.4 mm which is larger than the largest particle diameter, which results in a good accuracy of the measurement at $\pm 10\%$ for 0.2 – 0.4 W/(mK) [69].

5 Results

5.1 Finite element simulating validation

Four subsamples from each scanned natural sand are extracted to calculate the effective thermal conductivity using the finite element simulation. Fig. 12 shows that the thermal conductivity decreases with porosity, and this trend agrees with the results presented previously by Yun and Santamarina (2008) [65] and Narsilio et al (2010) [61]. Fig. 12 also reveals that the numerical values are higher than that from experimental measurements but in an acceptable range [61]. The overestimation may result from the contact condition in both physical testing and numerical simulation. The needle probe testing has an accuracy of $\pm 10\%$ [69] and the error of finite element simulation come from its limitation in capturing particle surface roughness and particle geometry irregularity [61].

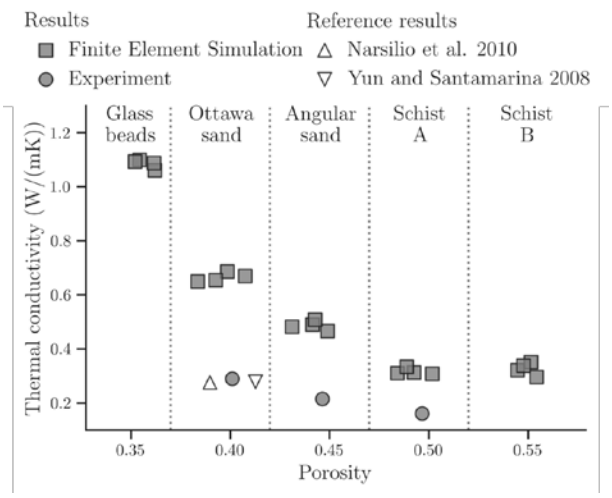

Fig. 12 The effective thermal conductivity of five natural sands from finite element simulations are larger than the experimental measurements, which may because numerical simulation does not capture particle surface roughness and particle geometry irregularity [51]

5.2 Effect of particle shape on thermal conductivity

A sub-sample X-ray CT image stack from each natural sand is selected to extract smooth individual particles using the framework summarised in Fig. 7. The average number of particles in each sub-sample is 150. This number of particles considered sufficiently representative for studies of uniform sands [20]. Within each sub-sample, for each smooth particle in it, its sphericity and roundness are calculated using S1 in Table 1 and Equation 5. Readers must recall that sphericity (S) and roundness (R) characterise particle shape at two different length scales: the overall form of the particle (S) and local features (i.e., the shape of “edges or corner” in the particle, R) as it can be seen in Fig. 1. Each coloured point in Fig. 13 corresponds to the calculated sphericity and roundness of each particle in the sub-sample assembly of particles. A particle shape chart [70] is also included as a background in Fig. 13 to provide a rough visualisation of the particle geometry. From Fig. 5, we already qualitatively know that the ascending ordering of angularity of the five sands is: Glass beads, Ottawa sand, Angular sand, Crushed schist A and Crushed schist B. In Fig. 13, we can also observe this trend: irregular particles have lower sphericity and roundness than more regular (and round) particles. Moreover, the range of sphericity and roundness in irregular sands have a wider distribution.

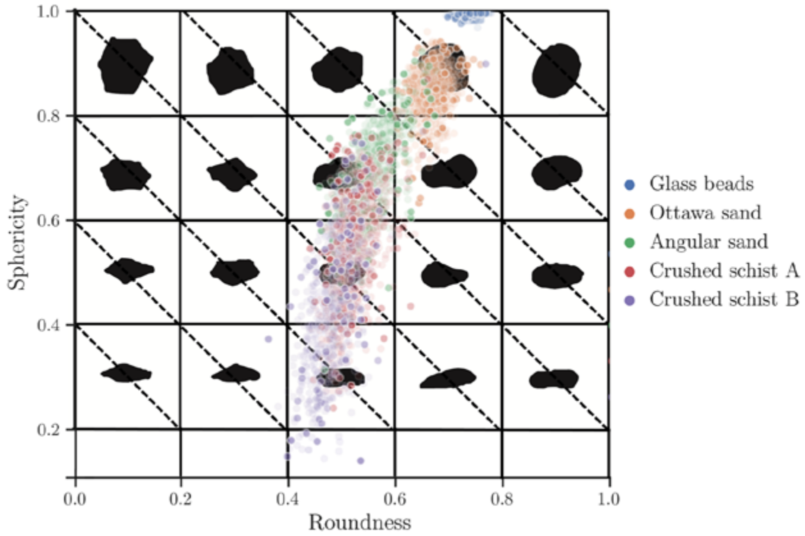

Fig. 13 Irregular particles have lower sphericity and roundness than round particles. Packings assembled by irregular particles have a wider range of sphericity and roundness. The background refers to [61]

After determining sphericity and roundness, their average can be used as a uniformed character of particle shape for the assembly of particles in each sub-sample [27]. The effect of particle shape on effective thermal conductivity can now be analysed with the quantitative particle shape descriptor. In this work, both the thermal conductivity of the five sands in dry and static water saturated conditions are computed as shown in Fig. 14 for five sub-samples of each sand. According to Fig. 14, the effective thermal conductivity increases when the average of sphericity and roundness increases. Furthermore, the trend in dry samples and water saturated samples are similar; however, the rate of increase in dry samples is slightly higher. The difference of the increasing rate may arise from the change in the main heat transfer pathways in the granular materials. As shown in Fig. 11 (c), the heat flux in *dry* granular materials is high at the particle contacts which is the main particle scale path for heat transfer in dry granular materials. However, the main heat transfer path in saturated sand is particle-fluid-particle whose contribution to the λ_{eff} is between 39.6% (in saturated Glass beads) and 74.1% (in saturated Crushed schist B). Since the pore space now is filled with water, the λ_{eff} of saturated Crushed shist B is around four times larger than the λ_{eff} of dry Crushed Schist B and larger than the λ_{eff} of dry Glass beads.

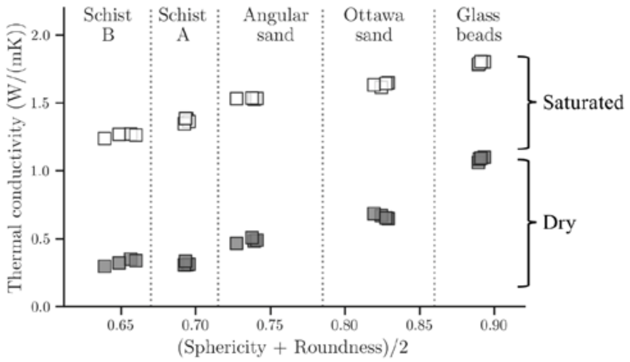

Fig. 14 Effective thermal conductivity increases when the average of sphericity and roundness increases in both dry (grey) and water saturated sands (white)

5.3 Effect of particle shape on microstructure

Since the inter-particle contact is the main heat transfer pathway in dry granular materials, coordination number and the inter-particle contact area are two microstructure properties believed to have a significant influence on the overall thermal conductivity. Accordingly, we further study the relationship between these two microstructure parameters and particle shape descriptors. After watershed segmentation (step 4 in Fig. 7), coordination number and contact area are calculated, and then the average coordination number and the average contact radius ratio for each microCT-ed sub-samples are calculated as well. The contact radius ratio is defined as the ratio between the radius of contact area and the radius of particles. Fig. 15 shows that both coordination number and contact radius ratio increase with the increase of the average value of sphericity and roundness, except for the Crushed schist B. Particles in the Crushed schist A and the Crushed schist B samples have similar average coordination number but Crushed schist B shows a higher average contact radius ratio, which may be because almost half of the particles in the Crushed schist B sample are platy and elongated (Fig. 13) particles resulting in larger interparticle contact areas. The increase of coordination number in the samples having more regular (round) particle coincide with the increment of λ_{eff} shown in Fig. 14. In general, the increase of contact ratio in more regular particle packings also coincide with the increment of λ_{eff} except for the packings containing very irregular and platy particles. These observations indicate the impact of particle shape represented by the three-dimensional sphericity and roundness on heat transfer in dry granular materials is more originated from its influence on the inter-particle contact number than on contact ratio (contact area).

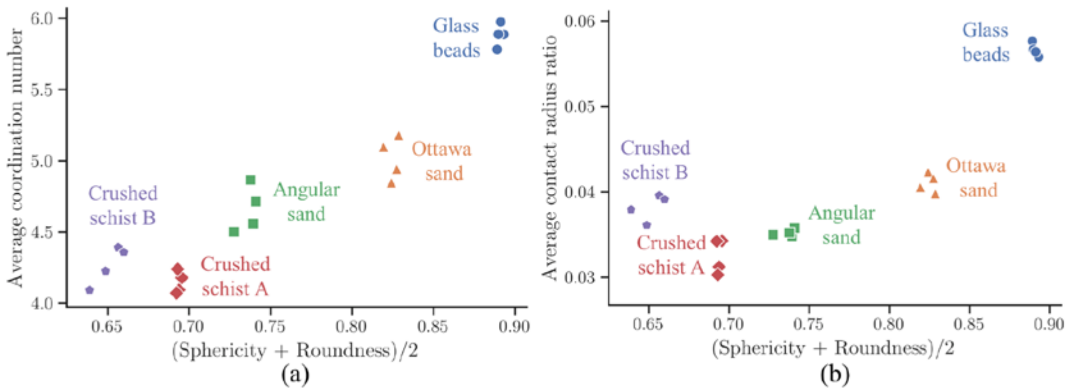

Fig. 15 Average contact radius ratio and average coordination number increase with the increment of the mean value of sphericity and roundness. (a) Average contact radius ratio and (b) Average coordination number

6 Conclusion

This study develops a method to calculate three-dimensional (3D) sphericity and roundness of individual particles in a specimen while preserving its internal structure. By comparing the existing definitions of 3D sphericity, a combination of sphericity and roundness is used to characterise particle shape. Sphericity and roundness are required to be calculated on a smooth particle surface which is achieved using a proposed framework including CT techniques, imaging techniques and the Tabuin smoothing method. The reliability of the smoothing framework is presented by its application to voxel-constructed sphere, ellipsoid, Ottawa sand particle and Angular sand particle.

By calculating the sphericity and roundness of individual particles in five natural sands, we found that irregular particles tend to show lower sphericity and roundness than more regular (and round) particles, and granular packings formed by irregular particles show a wider range of sphericity and roundness. Moreover, after estimating the thermal conductivity of the natural sands, we observed that granular materials with a higher average value of sphericity and roundness show a tendency to boost higher thermal conductivity. This is because we also found that lower average value of sphericity and roundness may lead to lower average coordination number and contact radius ratio, important parameters governing heat transfer at the particle scale. Granular assemblies containing more platy particles may exhibit higher average contact radius ratio compared to other assemblies with the same average coordination number. The five materials in this paper have different friction coefficients, the effect of the friction coefficient on the coordination number and contact ratio requires to be quantified in future work.

Acknowledgements

The authors acknowledge Yu Zhou for taking micro-photos of the sands. The CT images were obtained using the Imaging and Medical Beam Line (IMBL) at the Australian Synchrotron, Victoria, Australia. We acknowledge Dr. Anton Maksimenko and the other beam scientists at Australian Synchrotron for their support during our experiments. This work is supported by the Melbourne Research Scholarship from The University of Melbourne.

Reference

[1] A.E. Bergles, J. Collier, J.M. Delhaye, G. Hewitt, F. Mayinger, Two-phase flow and heat transfer in the power and process industries, Hemisphere New York1981.

[2] W.B. Fei, Q. Li, X.C. Wei, R.R. Song, M. Jing, X.C. Li, Interaction analysis for CO2 geological storage and underground coal mining in Ordos Basin, China, Engineering geology, 196 (2015) 194-209.

[3] D.M. Scott, D.K. Das, V. Subbaihaannadurai, V.A. Kamath, A computational scheme for fluid flow and heat transfer analysis in porous media for recovery of oil and gas, Petroleum science and technology, 23 (2005) 843-862.

[4] W.M. Rohsenow, J.P. Hartnett, E.N. Ganic, Handbook of heat transfer applications, New York, McGraw-Hill Book Co., 1985, 973 p. No individual items are abstracted in this volume., (1985).

[5] U. El Shamy, O. De Leon, R. Wells, Discrete element method study on effect of shear-induced anisotropy on thermal conductivity of granular soils, International Journal of Geomechanics, 13 (2013) 57-64.

[6] Y. Hu, J. Wang, J. Yang, I. Mudawar, Q. Wang, Experimental study of forced convective heat transfer in grille-particle composite packed beds, International Journal of Heat and Mass Transfer, 129 (2019) 103-112.

[7] J. Santamarina, G.-C. Cho, Soil behaviour: The role of particle shape, Advances in geotechnical engineering: The skempton conference, Citeseer, 2004, pp. 604-617.

[8] I. Cavarretta, M. Coop, C. O'Sullivan, The influence of particle characteristics on the behaviour of coarse grained soils, (2010).

[9] H. Shin, J. Santamarina, Role of particle angularity on the mechanical behavior of granular mixtures, Journal of Geotechnical and Geoenvironmental Engineering, 139 (2012) 353-355.

[10] T. Afshar, M.M. Disfani, A. Arulrajah, G.A. Narsilio, S. Emam, Impact of particle shape on breakage of recycled construction and demolition aggregates, Powder technology, 308 (2017) 1-12.

[11] A.B. Göktepe, A. Sezer, Effect of particle shape on density and permeability of sands, Proceedings of the Institution of Civil Engineers-Geotechnical Engineering, 163 (2010) 307-320.

[12] X. Garcia, L.T. Akanji, M.J. Blunt, S.K. Matthai, J.P. Latham, Numerical study of the effects of particle shape and polydispersity on permeability, Physical Review E, 80 (2009) 021304.

[13] A.F. Cabalar, N. Akbulut, Evaluation of actual and estimated hydraulic conductivity of sands with different gradation and shape, SpringerPlus, 5 (2016) 820.

[14] A. Banala, H. Ma, A. Kumar, Influence of particulate geometry on permeability of porous materials, Powder Technology, (2019).

[15] C. Lee, H.S. Suh, B. Yoon, T.S. Yun, Particle shape effect on thermal conductivity and shear wave velocity in sands, Acta Geotechnica, 12 (2017) 615-625.

[16] Y.F. Chen, M. Wang, S. Zhou, R. Hu, C.B. Zhou, An effective thermal conductivity model for unsaturated compacted bentonites with consideration of bimodal shape of pore size distribution, Science China Technological Sciences, 58 (2015) 369-380.

[17] J. Gan, Z. Zhou, A. Yu, Effect of particle shape and size on effective thermal conductivity of packed beds, Powder Technology, 311 (2017) 157-166.

[18] A.S. Cherkasova, J.W. Shan, Particle aspect-ratio effects on the thermal conductivity of micro-and nanoparticle suspensions, Journal of Heat Transfer, 130 (2008) 082406.

[19] G. Landini, Advanced shape analysis with ImageJ, Proceedings of the Second ImageJ user and developer Conference, Luxembourg, 2008, pp. 6-7.

[20] M.R. Cox, M. Budhu, A practical approach to grain shape quantification, Engineering Geology, 96 (2008) 1-16.

[21] H. Gerhardter, R. Prieler, C. Schluckner, M. Knoll, C. Hochenauer, M. Mühlböck, P. Tomazic, H. Schroettner, Modelling convective heat transfer to non-spherical particles, Powder Technology, 343 (2019) 245-254.

[22] R.L. Hamilton, O. Crosser, Thermal conductivity of heterogeneous two-component systems, Industrial & Engineering chemistry fundamentals, 1 (1962) 187-191.

[23] L. Verma, A. Shrotriya, R. Singh, D. Chaudhary, Thermal conduction in two-phase materials with spherical and non-spherical inclusions, Journal of Physics D: Applied Physics, 24 (1991) 1729.

[24] H. Wadell, Volume, shape, and roundness of rock particles, The Journal of Geology, 40 (1932) 443-451.
[25] S. Zhao, N. Zhang, X. Zhou, L. Zhang, Particle shape effects on fabric of granular random packing, Powder technology, 310 (2017) 175-186.
[26] D. Legland, I. Arganda-Carreras, P. Andrey, MorphoLibJ: integrated library and plugins for mathematical morphology with ImageJ, Bioinformatics, 32 (2016) 3532-3534.
[27] G. Cho, J. Dodds, J. Santamarina, Particle Shape Effects on Packing Density, Stiffness and Strength of Natural and Crushed Sands-Internal Report, Georgia Institute of Technology, 33pp, (2006).
[28] R.D. Hryciw, J. Zheng, K. Shetler, Particle roundness and sphericity from images of assemblies by chart estimates and computer methods, Journal of Geotechnical and Geoenvironmental Engineering, 142 (2016) 04016038.
[29] E.D. Sneed, R.L. Folk, Pebbles in the lower Colorado River, Texas a study in particle morphogenesis, The Journal of Geology, 66 (1958) 114-150.
[30] J.D. Frost, C.-T. Yang, Effect of end platens on microstructure evolution in dilatant specimens, Soils and foundations, 43 (2003) 1-11.
[31] L. Wang, J. Frost, J. Lai, Three-dimensional digital representation of granular material microstructure from X-ray tomography imaging, Journal of Computing in Civil Engineering, 18 (2004) 28-35.
[32] V. Cnudde, B. Masschaele, M. Dierick, J. Vlassenbroeck, L. Van Hoorebeke, P. Jacobs, Recent progress in X-ray CT as a geosciences tool, Applied Geochemistry, 21 (2006) 826-832.
[33] J. Neumann, J.-W. Simon, S. Reese, Digital sieving of irregular 3D particles—A study using XRCT and statistically similar synthetic data, Powder Technology, 338 (2018) 1001-1015.
[34] F. Cernuschi, C. Rothleitner, S. Clausen, U. Neuschaefer-Rube, J. Illemann, L. Lorenzoni, C. Guardamagna, H.E. Larsen, Accurate particle speed prediction by improved particle speed measurement and 3-dimensional particle size and shape characterization technique, Powder technology, 318 (2017) 95-109.
[35] Y. Lu, S. Xiao, Z. Ge, Z. Zhou, Y. Ling, L. Wang, Experimental study on rock-breaking performance of water jets generated by self-rotatory bit and rock failure mechanism, Powder Technology, 346 (2019) 203-216.
[36] G. Bagheri, C. Bonadonna, On the drag of freely falling non-spherical particles, Powder Technology, 301 (2016) 526-544.
[37] M. Aboufoul, A. Chiarelli, I. Triguero, A. Garcia, Virtual porous materials to predict the air void topology and hydraulic conductivity of asphalt roads, Powder Technology, 352 (2019) 294-304.
[38] J. Fonseca, C. O'Sullivan, M.R. Coop, P. Lee, Non-invasive characterization of particle morphology of natural sands, Soils and Foundations, 52 (2012) 712-722.
[39] T.S. Yun, J.C. Santamarina, Fundamental study of thermal conduction in dry soils, Granular matter, 10 (2008) 197.
[40] B. Zhao, J. Wang, M. Coop, G. Viggiani, M. Jiang, An investigation of single sand particle fracture using X-ray micro-tomography, Géotechnique, 65 (2015) 625-641.
[41] B. Zhou, J. Wang, H. Wang, Three-dimensional sphericity, roundness and fractal dimension of sand particles, Géotechnique, 68 (2017) 18-30.
[42] G. Kerckhofs, G. Pyka, M. Moesen, J. Schrooten, M. Wevers, High-resolution micro-CT as a tool for 3D surface roughness measurement of 3D additive manufactured porous structures, iCT Conf, 2012, pp. 77-83.
[43] J. Schindelin, I. Arganda-Carreras, E. Frise, V. Kaynig, M. Longair, T. Pietzsch, S. Preibisch, C. Rueden, S. Saalfeld, B. Schmid, Fiji: an open-source platform for biological-image analysis, Nature methods, 9 (2012) 676.
[44] M.d. Carmo, Differential geometry of curves and surfaces. 1976, Prentice-Hall, Englewood Cliffs, New Jersey). Rehsteiner, F. and Rewker, HJ Collision free five axis milling of twisted ruled surface. Ann. CIRP, 42 (1993) 457-461.
[45] P. Cignoni, M. Callieri, M. Corsini, M. Dellepiane, F. Ganovelli, G. Ranzuglia, Meshlab: an open-source mesh processing tool, Eurographics Italian chapter conference, 2008, pp. 129-136.
[46] ASTM, C778-17 standard specification for standard sand, ASTM International, West Conshohocken, PA, (2017).
[47] N. Zhang, X. Yu, A. Pradhan, A.J. Puppala, Thermal conductivity of quartz sands by thermo-time domain reflectometry probe and model prediction, Journal of Materials in Civil Engineering, 27 (2015) 04015059.
[48] K.K. Neuendorf, J.P. Mehl Jr, J.A. Jackson, Glossary of Geology: American Geological Institute, Alexandria, Virginia, (2005).

[49] A. VandenBerg, The Tasman Fold Belt system in Victoria: geology and mineralisation of Proterozoic to Carboniferous rocks, Geological Survey of Victoria2000.

[50] M. Wiebicke, E. Andò, I. Herle, G. Viggiani, On the metrology of interparticle contacts in sand from x-ray tomography images, Measurement Science and Technology, 28 (2017) 124007.

[51] P. Iassonov, T. Gebrenegus, M. Tuller, Segmentation of X-ray computed tomography images of porous materials: A crucial step for characterization and quantitative analysis of pore structures, Water Resources Research, 45 (2009).

[52] N. Otsu, A threshold selection method from gray-level histograms, IEEE transactions on systems, man, and cybernetics, 9 (1979) 62-66.

[53] S. Schlüter, A. Sheppard, K. Brown, D. Wildenschild, Image processing of multiphase images obtained via X-ray microtomography: a review, Water Resources Research, 50 (2014) 3615-3639.

[54] Z. Karatza, E. Andò, S. Papanicolopulos, J. Ooi, G. Viggiani, Evolution of deformation and breakage in sand studied using X-ray tomography, Géotechnique, 1 (2018) 1-11.

[55] H. Taylor, C. O'Sullivan, W. Sim, A new method to identify void constrictions in micro-CT images of sand, Computers and Geotechnics, 69 (2015) 279-290.

[56] G. Taubin, Curve and surface smoothing without shrinkage, Computer Vision, 1995. Proceedings., Fifth International Conference on, IEEE, 1995, pp. 852-857.

[57] A.G. Belyaev, Y. Ohtake, K. Abe, Detection of ridges and ravines on range images and triangular meshes, Vision Geometry IX, International Society for Optics and Photonics, 2000, pp. 146-155.

[58] Y. Ohtake, A. Belyaev, I. Bogaevski, Mesh regularization and adaptive smoothing, Computer-Aided Design, 33 (2001) 789-800.

[59] Y. Belyaev, H. Seidel, Mesh smoothing by adaptive and anisotropic Gaussian filter applied to mesh normals, Vision, modeling, and visualization, 2002, pp. 203-210.

[60] V. Tarnawski, T. Momose, W. Leong, Assessing the impact of quartz content on the prediction of soil thermal conductivity, Geotechnique, 59 (2009) 331-338.

[61] G.A. Narsilio, J. Kress, T.S. Yun, Characterisation of conduction phenomena in soils at the particle-scale: Finite element analyses in conjunction with synthetic 3D imaging, Computers and Geotechnics, 37 (2010) 828-836.

[62] G.A. Narsilio, O. Buzzi, S. Fityus, T.S. Yun, D.W. Smith, Upscaling of Navier–Stokes equations in porous media: Theoretical, numerical and experimental approach, Computers and Geotechnics, 36 (2009) 1200-1206.

[63] C. AB, COMSOL multiphysics v5.0, http://www.comsol.com, (2015).

[64] S. Ltd., Simpleware ScanIP, http://www.simpleware.com/software/scanip, Date of access, 15 (2015) 12.

[65] T.S. Yun, T.M. Evans, Three-dimensional random network model for thermal conductivity in particulate materials, Computers and Geotechnics, 37 (2010) 991-998.

[66] J. Sundberg, P.-E. Back, L.O. Ericsson, J. Wrafter, Estimation of thermal conductivity and its spatial variability in igneous rocks from in situ density logging, International Journal of Rock Mechanics and Mining Sciences, 46 (2009) 1023-1028.

[67] H.D. Young, R.A. Freedman, T. Sandin, A.L. Ford, University physics, Addison-Wesley Reading, MA1996.

[68] ASTM D5334-14, Standard Test Method for Determination of Thermal Conductivity of Soil and Soft Rock by Thermal Needle Probe Procedure, ASTM International, West Conshohocken, PA, 2014.

[69] T. Brandon, J. Mitchell, Factors influencing thermal resistivity of sands, Journal of Geotechnical Engineering, 115 (1990) 1683-1698.

[70] W.C. Krumbein, L.L. Sloss, Stratigraphy and sedimentation, 1963.